




# Synthesis of peanut-shaped porous ZnMn<sub>2</sub>O<sub>4</sub> microparticles with enhanced lithium storage properties

Fei Wang<sup>1,\*</sup> , Hanwen Dai<sup>1</sup>, Sheng Chen<sup>1</sup>, Jiaojiao Li<sup>1</sup>, and Yanming Wang<sup>2</sup>

<sup>1</sup>School of Chemistry and Materials Science, Huaibei Normal University, Huaibei 235000, Anhui, China

<sup>2</sup>Information College, Huaibei Normal University, Huaibei 235000, Anhui, China

Received: 18 August 2020

Accepted: 30 September 2020

Published online:

14 October 2020

© Springer Science+Business Media, LLC, part of Springer Nature 2020

## ABSTRACT

Peanut-shaped porous ZnMn<sub>2</sub>O<sub>4</sub> microparticles assembled by nanoparticles have been prepared by annealing treatment of the Zn<sub>1/3</sub>Mn<sub>2/3</sub>CO<sub>3</sub> precursors synthesized via a solvothermal reaction in water-triethanolamine binary solvent. The volume ratio of water to triethanolamine remarkably affects the shape and particle size of the carbonate precursor. The monodisperse ZnMn<sub>2</sub>O<sub>4</sub> microparticles with a length of ca. 1 μm and a width of ca. 0.5 μm are constructed by many interlinked nanoparticles with a size of ca. 50–90 nm. As anode materials for Li-ion batteries, the peanut-shaped ZnMn<sub>2</sub>O<sub>4</sub> microparticles display an outstanding rate capability with a lithiation capacity of 579 mAh g<sup>-1</sup> at 4 A g<sup>-1</sup> and long-cycle performance with a reversible capacity of 797 mAh g<sup>-1</sup> after 700 cycles at 0.5 A g<sup>-1</sup>. The significantly enhanced lithium storage properties benefit from the desired porous micro-/nanostructures with suitable particle sizes, which enable the fast diffusion for lithium ions and the structural integrity of the electrode upon cycling.

## 1 Introduction

In recent decades, rechargeable Li-ion batteries (LIBs) have been extensively employed for modern mobile electronics due to their virtues of high voltage, long lifespan, and environmentally benign nature [1, 2]. Nonetheless, commercialized graphite anode offers a limited theoretical specific capacity (372 mAh g<sup>-1</sup>), hampering its practical application for advanced LIBs as well as the future electric vehicles (EVs) [3, 4].

Recently, transition metal oxides (TMOs) have emerged as candidates to replace the traditional graphite owing to their much higher theoretical capacities [5–7]. In contrast to single-component oxides, spinel mixed transition metal oxides, such as ZnMn<sub>2</sub>O<sub>4</sub>, ZnFe<sub>2</sub>O<sub>4</sub>, ZnCo<sub>2</sub>O<sub>4</sub>, MnCo<sub>2</sub>O<sub>4</sub>, etc., have been exploited as anode materials, owing to the complementary and synergetic effects caused by mixed metal cations, which can bring better electrical

Address correspondence to E-mail: wangfeichem@126.com

conductivity and electrochemical performances [8–11].

Among different transition metal oxides, tetragonal  $\text{ZnMn}_2\text{O}_4$  holds promise as a competitive anode for LIBs. On one hand, both Zn and Mn resources are low-priced, eco-friendly, and abundant in nature with respect to many other metals [12, 13]. On the other hand, as an anode for LIBs,  $\text{ZnMn}_2\text{O}_4$  provides a larger energy density on account of its large theoretical lithiation capacity ( $784 \text{ mAh g}^{-1}$ ) and low oxidation potential ( $\sim 1.2 \text{ V vs. Li}^+/\text{Li}$ ) [14, 15]. Nevertheless, like other transition metal oxides,  $\text{ZnMn}_2\text{O}_4$  suffers from drastic volume variation throughout the repeated lithiation/delithiation processes, which gradually results in the destruction of electrode structure and an inevitable capacity fade [16, 17]. To overcome this problem, porous structured  $\text{ZnMn}_2\text{O}_4$  has been designed and fabricated so as to alleviate the stress and strain induced by volume variation and thereby improve the structural stability [18]. For example, Dang et al. [19] constructed uniform  $\text{ZnMn}_2\text{O}_4$  porous microspheres via a solvothermal method, which provided a discharge capacity of  $602 \text{ mAh g}^{-1}$  after 100 cycles at  $100 \text{ mA g}^{-1}$ . Rong et al. [20] adopted a two-step synthesis route to obtain porous nanoparticle-composed  $\text{ZnMn}_2\text{O}_4$  microspheres, delivering a specific capacity of  $724 \text{ mAh g}^{-1}$  at 350th cycle at  $400 \text{ mA g}^{-1}$ . Wang et al. [21] synthesized porous  $\text{ZnMn}_2\text{O}_4$  microspheres composed of interconnected nanoparticles, which preserved a steady capacity of  $800 \text{ mAh g}^{-1}$  after 300 cycles. Except for various types of microspheres, other porous structured  $\text{ZnMn}_2\text{O}_4$  is rare and thus has great research potential.

We report herein novel peanut-shaped porous  $\text{ZnMn}_2\text{O}_4$  microparticles, which are prepared by annealing treatment of  $\text{Zn}_{1/3}\text{Mn}_{2/3}\text{CO}_3$  precursors synthesized by using a triethanolamine-assisted solvothermal reaction. Triethanolamine (TEA) acts as both the reaction solvent and surfactant during the solvothermal reaction process. The particle size and shape of  $\text{Zn}_{1/3}\text{Mn}_{2/3}\text{CO}_3$  vary with the volume ratio of water to TEA. As a result, a uniform peanut-shaped microstructure can be formed in the water-TEA (1:1, v/v) mixture. After thermal decomposition in air, the nanoparticle-composed peanut-shaped  $\text{ZnMn}_2\text{O}_4$  microparticles are well formed and possess plenty of void space. As anode materials for LIBs, the  $\text{ZnMn}_2\text{O}_4$  micro-/nanostructures illustrate outstanding rate capability and long-term cycling stability.

## 2 Experimental section

### 2.1 Preparation of $\text{ZnMn}_2\text{O}_4$ microparticles

Firstly, 1 mmol zinc acetate dihydrate, 2 mmol manganese acetate tetrahydrate and 0.06 mol urea were dissolved in 30 mL of deionized water and TEA (1:1, v/v) under continuous stirring for 0.5 h. Secondly, the resultant homogeneous solution was placed in a 50 mL Teflon-lined autoclave and heated to  $160 \text{ }^\circ\text{C}$  for 12 h, resulting in the formation of the  $\text{Zn}_{1/3}\text{Mn}_{2/3}\text{CO}_3$  precursors. Then the white precursors were collected by centrifugal separation and washed alternately with deionized water and alcohol. After drying, the  $\text{Zn}_{1/3}\text{Mn}_{2/3}\text{CO}_3$  precursors were calcined at  $600 \text{ }^\circ\text{C}$  in air for 5 h to obtain the final  $\text{ZnMn}_2\text{O}_4$  products. To understand the influence of solvent medium on the formation of the precursors, the solvothermal reactions using various volume ratios of deionized water to TEA (30:0, 25:5, 20:10, 10:20 and 5:25) were performed for comparison under the same experimental conditions.

### 2.2 Materials characterizations

The crystal phase was measured by X-ray diffraction (XRD) (PANalytical X'pert Pro) in the  $2\theta$  range of  $10^\circ$ – $80^\circ$ . The morphologies and microstructures were detected through scanning electron microscope (SEM) (Phenom ProX) and field-emission transmission electron microscope (TEM) (FEI, Tecnai G2 F20). Brunauer-Emmett-Teller (BET) characterization and pore size analysis were characterized via Nitrogen adsorption-desorption isotherms at 77 K using Micromeritics ASAP 2460. X-ray photoelectron spectroscopy (XPS) was carried out on an AXIS Ultra DLD spectrometer with Al-K $\alpha$  radiation.

### 2.3 Electrochemical measurements

The anode performances of the  $\text{ZnMn}_2\text{O}_4$  microparticles were tested with CR2016-type coin cells under room temperature using lithium metal as the counter/reference electrode and Celgard 2400 film as the separator. The working electrode consisted of 70 wt%  $\text{ZnMn}_2\text{O}_4$ , 20 wt% Super P, and 10 wt% polyvinylidene fluoride. The mass loading of active materials is ca.  $1 \text{ mg cm}^{-2}$  in the electrode. The electrolyte solution was 1 M  $\text{LiPF}_6$  in a mixture of 50 wt% ethylene carbonate and 50 wt% dimethyl carbonate. The cells

assembled in an argon-filled glove box were set quietly for 4 h, and then cycled between 0.01 and 3.0 V on a battery testing system (LANHE CT2001). Cyclic voltammetry (CV) was tested by an electrochemical workstation (CHI750E) with a scan rate of  $0.1 \text{ mV s}^{-1}$ .

### 3 Results and discussion

Figure 1a exhibits the XRD pattern of the  $\text{Zn}_{1/3}\text{Mn}_{2/3}\text{CO}_3$  precursor, which can be indexed as a solid mixture of  $\text{ZnCO}_3$  and  $\text{MnCO}_3$  because of the similar crystal structure and close lattice constants [21, 22]. After annealing treatment of the precursor, all diffraction peaks of the product (Fig. 1b) can be assigned to the tetragonal spinel-phase  $\text{ZnMn}_2\text{O}_4$  (JCPDS card no. 24-1133). The high peak density and no detectable peaks from impurities suggest that the resultant  $\text{ZnMn}_2\text{O}_4$  has good crystallinity and high purity.

The elemental composition and metallic oxidation states of the  $\text{ZnMn}_2\text{O}_4$  product were determined by XPS characterization, as shown in Fig. 2. The survey spectrum (Fig. 2a) confirms the existence of Zn, Mn and O as well as C elements, of which the C 1 s peak acts as the reference for calibration. In Fig. 2b, two sharp peaks centered at binding energies of 1044.5 eV for Zn 2p<sub>1/2</sub> and 1021.4 eV for Zn 2p<sub>3/2</sub> with the binding energy difference of 23.1 eV indicate the presence of Zn<sup>2+</sup> ion in  $\text{ZnMn}_2\text{O}_4$  [4, 7]. In Fig. 2c, two strong peaks loaded at binding energies of

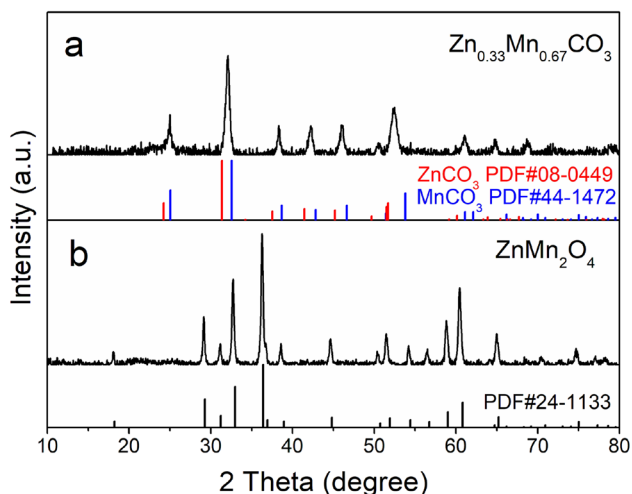


**Fig. 1** XRD patterns of the  $\text{Zn}_{1/3}\text{Mn}_{2/3}\text{CO}_3$  precursor (a) and  $\text{ZnMn}_2\text{O}_4$  product (b)

654.0 eV for Mn 2p<sub>1/2</sub> and 642.2 eV for Mn 2p<sub>3/2</sub> with the binding energy difference of 23.1 eV illustrate the existence of Mn<sup>3+</sup> ion [12, 16]. As depicted in Fig. 2d, the O 1 s spectrum could be divided into two peaks at 530.1 eV and 531.8 eV, corresponding to the lattice oxygen and physically adsorbed oxygen, respectively [12, 20]. The above results are well in accordance with previously reported  $\text{ZnMn}_2\text{O}_4$  materials.

The SEM image (Fig. 3a) of the  $\text{ZnMn}_2\text{O}_4$  product reveals that a large quantity of uniform peanut-shaped microparticles are obtained with the width of ca. 0.5  $\mu\text{m}$  and the length of ca. 1  $\mu\text{m}$ . As shown in a high-magnification SEM image (Fig. 3b), the monodisperse microparticles are composed of tremendous interconnected nanoparticles with the size ranging from 50 to 90 nm. Moreover, the microparticles possess specific porous structure, resulting from the carbonate pyrolysis with release of  $\text{CO}_2$ . The contrast of bright and shade in the TEM image (Fig. 3c) further confirms the homogeneously distributed pores inside the  $\text{ZnMn}_2\text{O}_4$  microparticles. The HRTEM image displays the distinct lattice fringes with an interplanar spacing of 0.25 nm, corresponding to the  $\text{ZnMn}_2\text{O}_4$  (211) plane (Fig. 3d) [7].

The influences of solvent composition on the shape and particle size of the carbonate precursor have been further investigated. Figure 4a–f illustrate the SEM images of the precursors synthesized employing different volume ratios of water to TEA. As seen in Fig. 4a, cubical and spherical particles beyond the size of 10  $\mu\text{m}$  could be achieved when using pure water as the solvent. With the increase of TEA content in the water-TEA mixed solvent, the cubes gradually disappeared and the spheres grew into the strips (Fig. 4b, c). Meanwhile, the particle size of the precursor reduced rapidly. When the TEA percentage reached 50%, the precursor particles became regular peanut-shape with lengths of ca. 1  $\mu\text{m}$  (Fig. 4d). Presumably TEA may work as the surfactant to regulate and control the crystal growth of  $\text{Zn}_{1/3}\text{Mn}_{2/3}\text{CO}_3$  because the hydroxyl and amine groups in TEA molecules could be selectively adsorbed onto the crystal surface [23–25]. However, with the increasing TEA content, the peanut-shaped particles grew into irregular and larger spheres again (Fig. 4e, f). Note that the certain amount of water in the urea-assisted solvothermal reaction is crucial to the shape and even purity of the precursors at the same time [26]. Consequently, TEA and water have a strong synergistic effect on the formation of a peanut-shaped

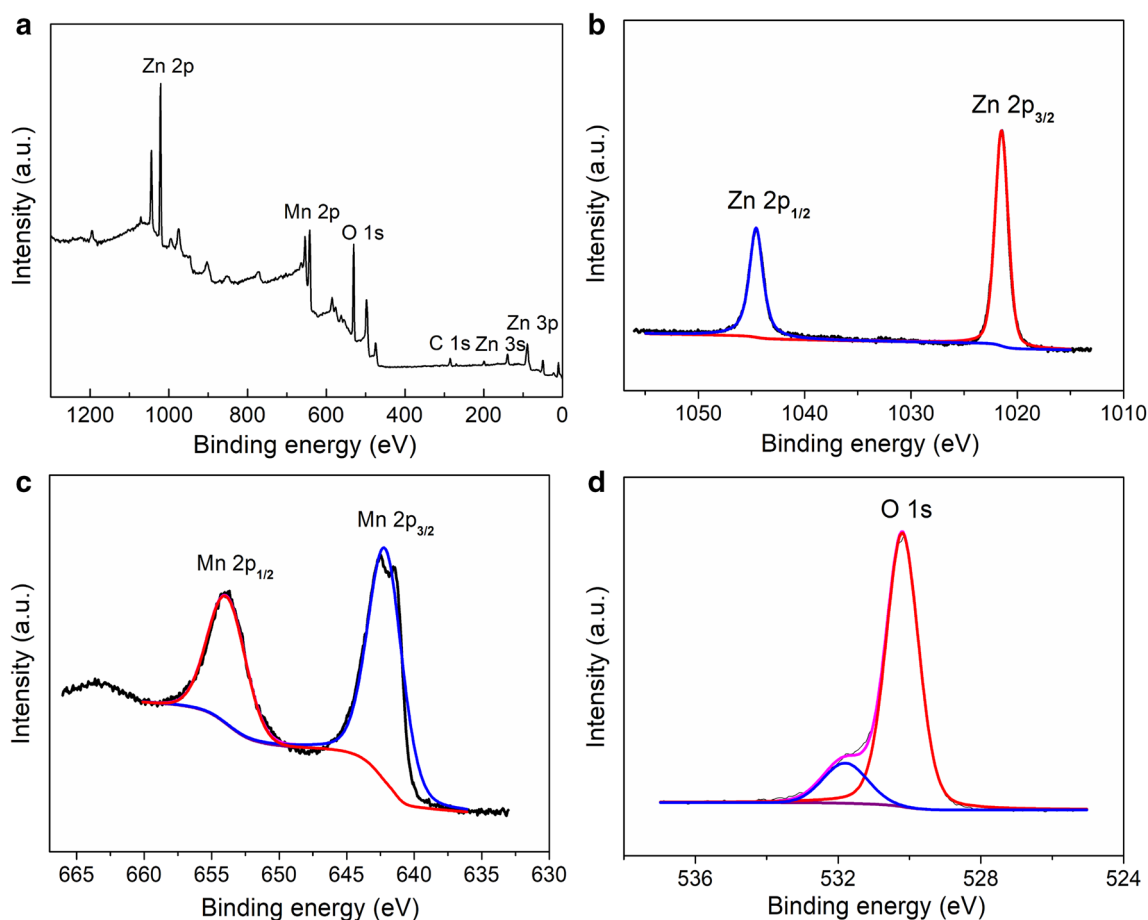


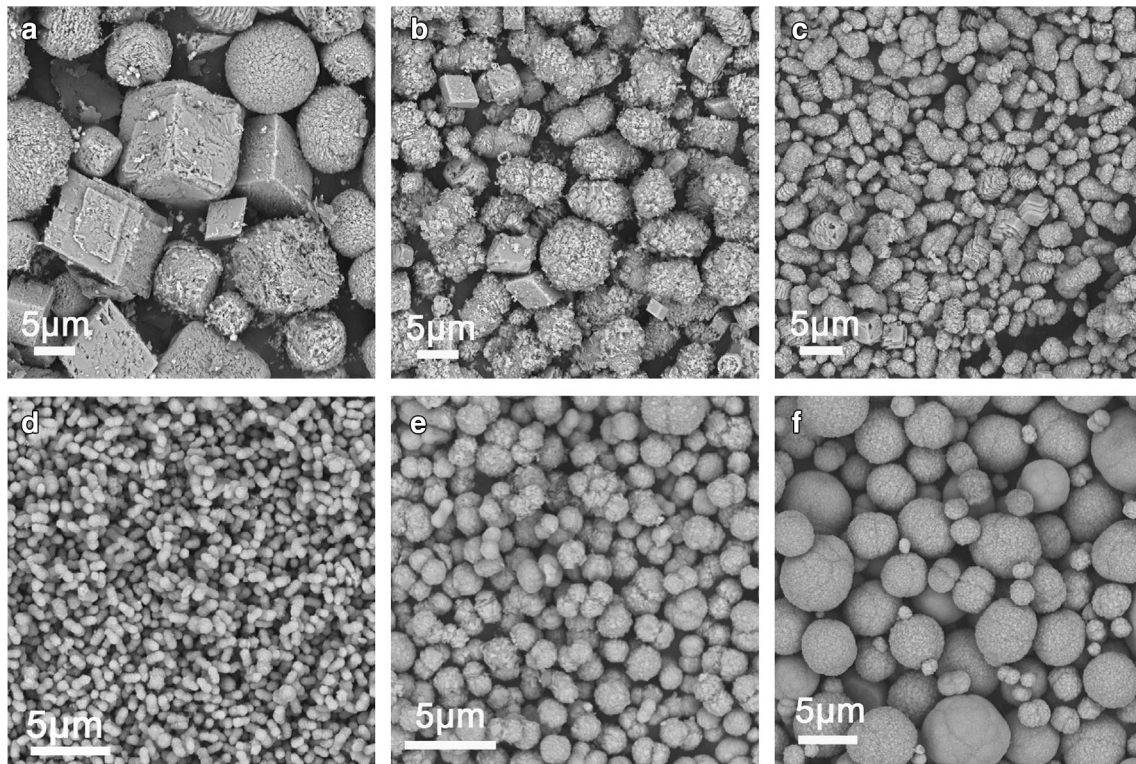
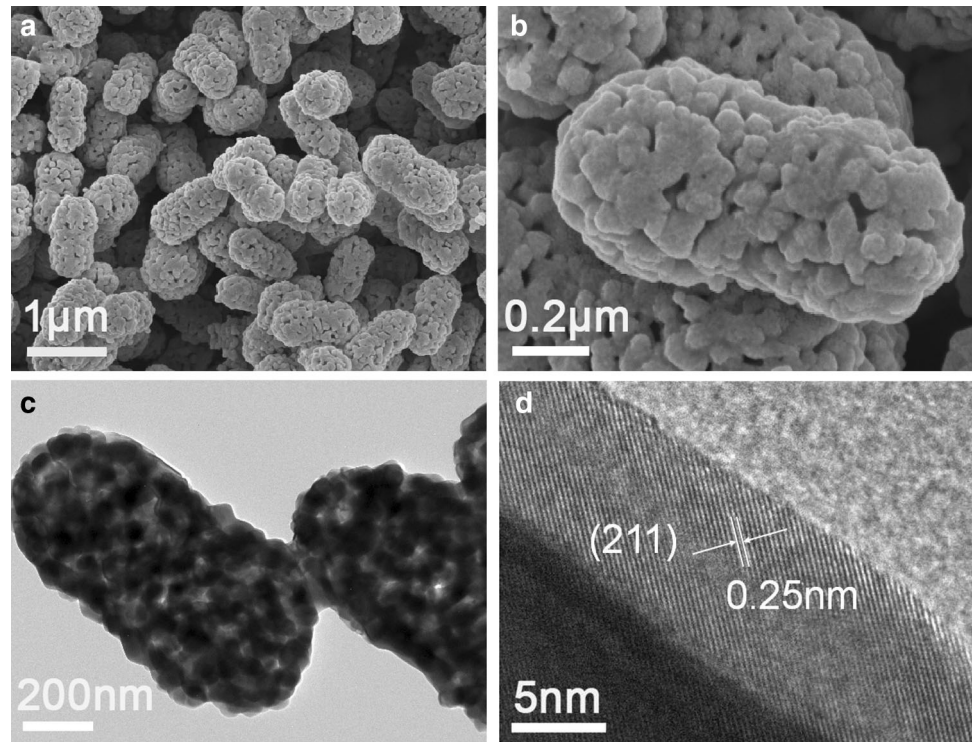
**Fig. 2** XPS spectra of survey spectrum, a Zn 2p (b), Mn 2p (c), and O 1s (d) of the  $\text{ZnMn}_2\text{O}_4$  product

micro/nanostructure with homogeneous shape and small particle size.

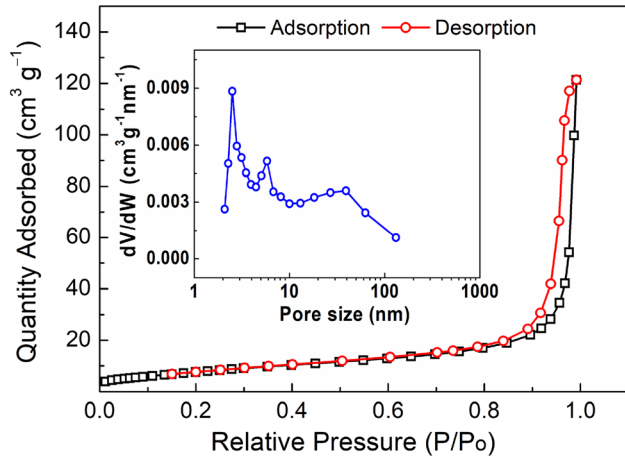
The porous characteristic and BET surface area of the peanut-shaped  $\text{ZnMn}_2\text{O}_4$  microparticles were investigated by the nitrogen adsorption/desorption isotherm and Barrett-Joyner-Halenda (BJH) method, as shown in Fig. 5. The isotherm with a hysteresis loop can be classified as a type-IV curve, suggesting the existence of mesoporous structure [8, 9]. The resultant surface area is calculated as large as  $29.3 \text{ m}^2 \text{ g}^{-1}$  with total pore volume of  $0.19 \text{ cm}^3 \text{ g}^{-1}$ . The pore size distributes in the range of 2–90 nm with an average pore width of 26.7 nm. Such a benign porous structure with a large surface area could not only provide the buffer space to alleviate the structural expansion during lithiation process, but also greatly facilitate the fast  $\text{Li}^+$  ion transport at the electrode/electrolyte interface, thus bringing about good electrochemical performance [27–29].

Figure 6a gives the initial five successive CV profiles between 0.01 and 3.0 V. In the 1st cathodic scan, two peaks at 1.21 V and 0.70 V, disappearing during the following scans, are ascribed to the reduction of  $\text{Mn}^{3+}$  to  $\text{Mn}^{2+}$  and the generation of a solid electrolyte interphase (SEI) layer, respectively [3]. In addition, the strong peak centered at 0.26 V is caused by the reduction of  $\text{Zn}^{2+}/\text{Mn}^{2+}$  to Zn/Mn and the subsequent Li–Zn alloying reaction [30]. The 1st anodic process exhibits a wide peak close to 1.28 V corresponding to the oxidation of Mn/Zn to  $\text{Mn}^{2+}/\text{Zn}^{2+}$  [31]. The cathodic reduction peaks in the 2nd to 5th cycles positively shift to ca. 0.35 V, resulting from the irreversible electrode reactions in the 1st cycle. The CV curves after the initial cycle are gradually overlapped, revealing a high electrochemical reversibility of the  $\text{ZnMn}_2\text{O}_4$  anode. The lithiation/delithiation process can be processed as follows [3, 5, 22]:

**Fig. 3** SEM images (a, b), TEM image (c) and HRTEM image (d) of the peanut-shaped porous  $\text{ZnMn}_2\text{O}_4$  microparticles



**Fig. 4** SEM images of  $\text{Zn}_{1/3}\text{Mn}_{2/3}\text{CO}_3$  precursors prepared with various volume ratios of water to TEA: a 30:0, b 25:5, c 20:10, d 15:15, e 10:20, and f 5:25



**Fig. 5** Nitrogen adsorption/desorption isotherm and BJH pore size distribution (inset) for the peanut-shaped porous ZnMn<sub>2</sub>O<sub>4</sub>

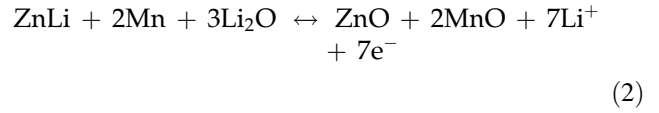
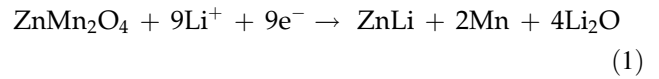
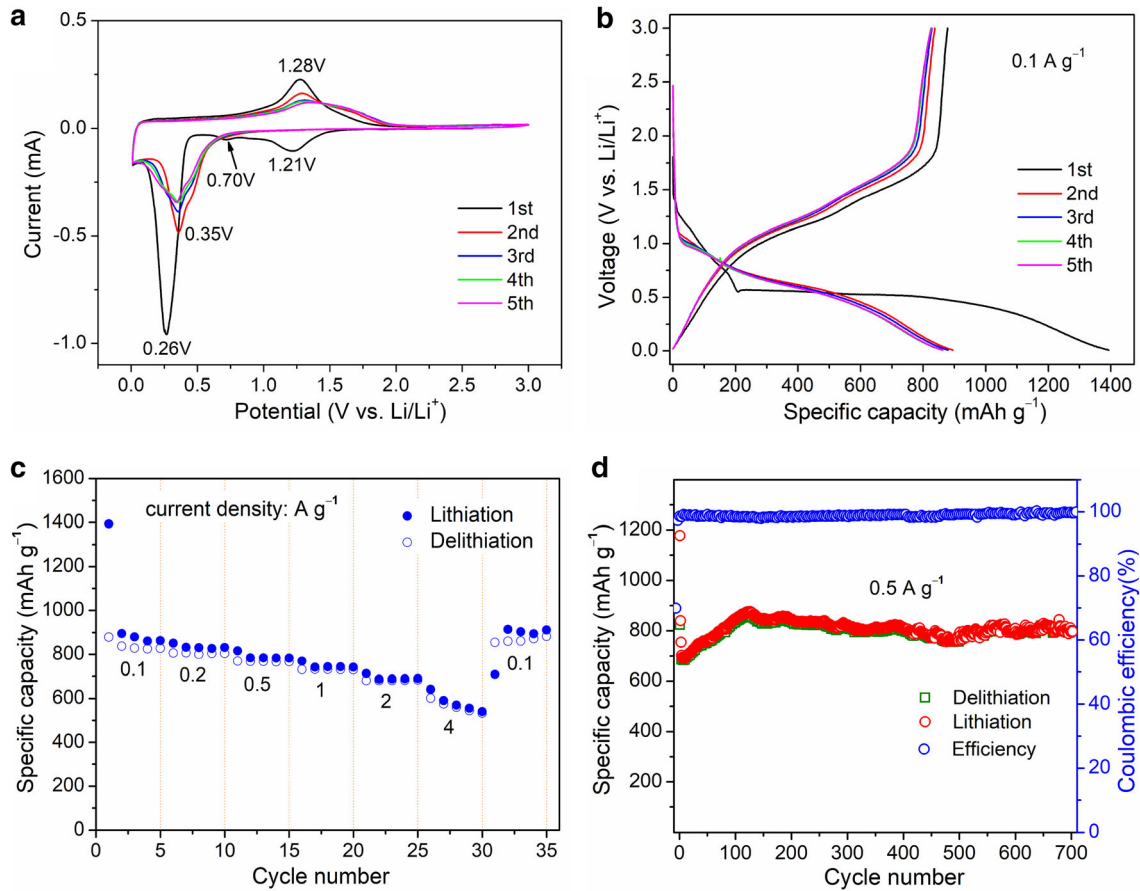
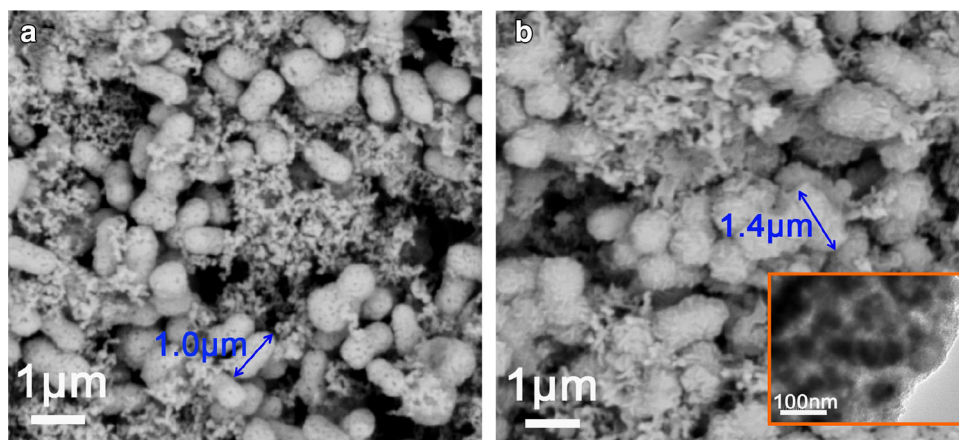


Figure 6b presents the voltage profiles of the peanut-shaped porous ZnMn<sub>2</sub>O<sub>4</sub> microparticle anode at a specific current of 0.1 A g<sup>-1</sup> in the first five cycles. The porous ZnMn<sub>2</sub>O<sub>4</sub> anode exhibits the initial lithiation and delithiation capacities of 1393 mAh g<sup>-1</sup> and 878 mAh g<sup>-1</sup> with a coulombic efficiency of 63%. The large irreversible capacity loss may basically be



**Fig. 6** CV profiles (a), voltage profiles (b), cycling stability (c), and rate performance (d) of the ZnMn<sub>2</sub>O<sub>4</sub> anode

**Fig. 7** SEM image of the  $\text{ZnMn}_2\text{O}_4$  microparticles before cycling (a) and after 100 cycles (The inset shows its TEM image) (b)



induced by the formation of SEI film on the electrode interface and irreversible consumption of  $\text{Li}^+$  in the defects of the  $\text{ZnMn}_2\text{O}_4$  particles [21, 32]. Particularly, all the voltage plateaus and the finally overlapped voltage profiles conform well to the CV data. The coulombic efficiency rapidly approaches more than 96% in the 4th cycle, indicating a good lithium insertion/removal reversibility of the  $\text{ZnMn}_2\text{O}_4$  anode.

Figure 6c depicts the rate performance of the peanut-shaped  $\text{ZnMn}_2\text{O}_4$  anode. The average lithiation capacities of 879, 831, 783, 743, 688, and 579  $\text{mAh g}^{-1}$  are obtained at specific currents of 0.1, 0.2, 0.5, 1, 2, and 4  $\text{A g}^{-1}$ , respectively. The reversible capacity at a high specific current of 4  $\text{A g}^{-1}$  is about 1.5 times the theoretical capacity of the commercialized graphite, which demonstrates that the as-prepared  $\text{ZnMn}_2\text{O}_4$  anode has great application potential for high-power LIBs. Particularly, a high lithiation capacity of 903  $\text{mAh g}^{-1}$  can still be obtained when the specific current returns to 0.1  $\text{A g}^{-1}$ , indicating the good electrode reaction reversibility. It is believed that the good rate capability of the  $\text{ZnMn}_2\text{O}_4$  anode results from its reasonable hierarchical micro-/nanosstructure and appropriate particle size. The secondary microparticles can make a good contact with conductive carbon in the electrode due to the oblong shape and relatively small size (ca. 1  $\mu\text{m}$ ), facilitating the improvement of electronic conductivity of active materials [23]. The small particle size of the primary nanoparticles offers short diffusion length for  $\text{Li}^+$  and large electrode reaction interface [33]. The rich pores on the surface and inside the microparticles permit the easy permeation of electrolyte into the whole micro-/nanosstructured active materials [34, 35]. All of the abovementioned factors are favorable for faster

electrochemical kinetics, resulting in the high-rate lithium storage performance.

The  $\text{ZnMn}_2\text{O}_4$  anode also exhibits good long-term cycling performance, as described in Fig. 6d. At a specific current of 0.5  $\text{A g}^{-1}$ , the lithiation capacity rapidly decreases from 840  $\text{mAh g}^{-1}$  for the 2nd cycle to 690  $\text{mAh g}^{-1}$  for the 6th cycle, and then gradually rises to a maximum value of 875  $\text{mAh g}^{-1}$  for the 125th cycle. Afterwards, the capacity decreases very slightly in the following cycles and maintains at 797  $\text{mAh g}^{-1}$  after 700 cycles with the coulombic efficiency retaining at 99% throughout the long-term cycling. A decrease followed by an increase in capacity has also been observed for other porous structured TMOs anodes [13]. The quick capacity decay is most likely related to the partial fracture and electrical isolation of the nanoparticles because of the large volume swelling during lithium insertion process [33]. The gradual capacity rise in subsequent cycles is attributable to the reactivation of the electrode, including the reconstruction of the interconnected three-dimensional porous structures and the reversible formation of a polymeric gel-like film on the anode surface [28, 29]. SEM images of the peanut-shaped porous  $\text{ZnMn}_2\text{O}_4$  microparticles before cycling and after 100 cycles at 0.5  $\text{A g}^{-1}$  are compared in Fig. 7a, b. After cycling, the particle size of  $\text{ZnMn}_2\text{O}_4$  increases to ca. 1.4 times that of the fresh particles due to the irreversible volume expansion and microstructure reconstruction throughout the continuous lithiation/delithiation reactions. More importantly, the peanut-shaped microparticle morphology is basically preserved without obvious destruction, resulting from the strong porous structure that effectively buffers the volume change. The TEM image (inset in Fig. 7b) also illustrates the

**Table 1** Electrochemical comparison of ZnMn<sub>2</sub>O<sub>4</sub> microparticles with other ZnMn<sub>2</sub>O<sub>4</sub> microspheres

Morphology of ZnMn <sub>2</sub> O <sub>4</sub>	Rate capability (mAh g <sup>-1</sup> )	Cycling property (mAh g <sup>-1</sup> )	References
Peanut-like porous microparticles	688 at 2 A g <sup>-1</sup> 579 at 4 A g <sup>-1</sup>	797 at 0.5 A g <sup>-1</sup> (700th)	This work
Porous microspheres	561 at 1.2 A g <sup>-1</sup>	493 at 0.2 A g <sup>-1</sup> (100th)	[5]
Porous microspheres	458 at 2 A g <sup>-1</sup>	~ 470 at 2 A g <sup>-1</sup> (500th)	[15]
Porous microspheres	484 at 1 A g <sup>-1</sup>	726 at 0.5 A g <sup>-1</sup> (90th)	[17]
Porous microspheres	483 at 0.5 A g <sup>-1</sup>	602 at 0.1 A g <sup>-1</sup> (100th)	[19]
Porous microspheres	422 at 2.5 A g <sup>-1</sup>	~ 650 at 0.4 A g <sup>-1</sup> (350th)	[20]
Porous microspheres	395 at 2 A g <sup>-1</sup>	800 at 0.5 A g <sup>-1</sup> (300th)	[21]
Porous nanospheres	~ 380 at 4 A g <sup>-1</sup>	800 at 0.2 A g <sup>-1</sup> (120th)	[22]
Porous microspheres	361 at 1.6 A g <sup>-1</sup>	607 at 0.4 A g <sup>-1</sup> (100th)	[36]
Porous microspheres	296 at 1 A g <sup>-1</sup>	745 at 0.2 A g <sup>-1</sup> (160th)	[37]
Porous microspheres	561 at 1.2 A g <sup>-1</sup>	820 at 0.5 A g <sup>-1</sup> (500th)	[38]

existence of void space inside the microparticle and interconnection of the nanoparticles after repeated cycles. Therefore, the outstanding structural stability of the porous micro-/nanostructure during cycling provides a long cycling life. As shown in Table 1, such remarkable electrochemical performances make the peanut-shaped porous ZnMn<sub>2</sub>O<sub>4</sub> microparticle a more promising anode material compared with some previously reported porous ZnMn<sub>2</sub>O<sub>4</sub> microspheres [5, 15, 17, 19–22, 36–38].

## 4 Conclusions

Herein, we report peanut-shaped porous ZnMn<sub>2</sub>O<sub>4</sub> microparticles synthesized through a facile solvothermal reaction and post-calcination method. The shape and size of the carbonate precursor can be adjusted by changing the solvent composition, i.e. the volume ratio of water to triethanolamine. Owing to the uniform porosity inside the micro-/nanostructure and the relatively small size of nanoparticle-composed microparticle, the ZnMn<sub>2</sub>O<sub>4</sub> microparticles not only accommodate the volume expansion over the repeated cycling, but also effectively facilitate the rapid Li<sup>+</sup> transport at the same time. As expected, the ZnMn<sub>2</sub>O<sub>4</sub> anode exhibits high lithiation capacities of 579 mAh g<sup>-1</sup> at 4 A g<sup>-1</sup> and 797 mAh g<sup>-1</sup> up to 700 cycles at 0.5 A g<sup>-1</sup>. The outstanding electrochemical performance validates our novel peanut-shaped

porous ZnMn<sub>2</sub>O<sub>4</sub> microparticle a competitive anode material for high-energy LIBs.

## Acknowledgements

This work was supported by Anhui Provincial Natural Science Foundation (Grant Nos. 1908085MB46, 2008085MB34), University Natural Science Research Project of Anhui Province (Grant No. KJ2018ZD058), and Outstanding Young Talents Program of Anhui University (Grant No. gxyqZD2019096).

## Compliance with ethical standards

**Conflict of interest** The authors declare that they have no conflict of interest.

## References

1. T.-F. Yi, T.-T. Wei, Y. Li, Y.-B. He, Z.-B. Wang, *Energy Storage Mater.* **26**, 165–197 (2020)
2. Z. Shen, Z. Zhang, S. Wang, Z. Liu, L. Wang, Y. Bi, Z. Meng, *Inorg. Chem. Front.* **6**, 3288–3294 (2019)
3. Z. Zhao, G. Tian, A. Sarapulova, V. Trouillet, Q. Fu, U. Geckle, H. Ehrenberg, S. Dsoke, *J. Mater. Chem. A* **6**, 19381–19392 (2018)
4. S. Chen, M. Yao, F. Wang, J. Wang, Y. Zhang, Y. Wang, *Ceram. Int.* **45**, 5594–5600 (2019)
5. D. Cai, D. Wang, H. Huang, X. Duan, B. Liu, L. Wang, Y. Liu, Q. Li, T. Wang, *J. Mater. Chem. A* **3**, 11430–11436 (2015)
6. J. Li, Y. Zhang, L. Li, Y. Wang, L. Zhang, B. Zhang, F. Wang, B. Li, X. Yu, *Dalton Trans.* **48**, 17022–17028 (2019)



7. S. Zhu, Q. Chen, C. Yang, Y. Zhang, L. Hou, G. Pang, X. He, X. Zhang, C. Yuan, *Int. J. Hydrogen Energy* **42**, 14154–14165 (2017)
8. J. Li, Y. Zhang, L. Li, L. Cheng, S. Dai, F. Wang, Y. Wang, X. Yu, *Sustain. Energy Fuels* **3**, 3370–3374 (2019)
9. D. Feng, H. Yang, X. Guo, *Chem. Eng. J.* **355**, 687–696 (2019)
10. Y. Wang, J. Li, S. Chen, B. Li, G. Zhu, F. Wang, Y. Zhang, *Inorg. Chem. Front.* **5**, 559–567 (2018)
11. H. Yang, Y. Xie, M. Zhu, Y. Liu, Z. Wang, M. Xu, S. Lin, *Dalton Trans.* **48**, 9205–9213 (2019)
12. Q. Gao, Z. Yuan, L. Dong, G. Wang, X. Yu, *Electrochim. Acta* **270**, 417–425 (2018)
13. X. Zhong, X. Wang, H. Wang, Z. Yang, Y. Jiang, J. Li, Z. Tian, *Nano Res.* **11**, 3814–3823 (2018)
14. Z. Zheng, Y. Cheng, X. Yan, R. Wang, P. Zhang, *J. Mater. Chem. A* **2**, 149–154 (2014)
15. T. Zhang, H. Yue, H. Qiu, Y. Wei, C. Wang, G. Chen, D. Zhang, *Nanotechnology* **28**, 105403 (2017)
16. B.C. Sekhar, P. Packiyalakshmi, N. Kalaiselvi, *ChemElectroChem* **4**, 1154–1164 (2017)
17. T. Ni, Y. Zhong, J. Sunarso, W. Zhou, R. Cai, Z. Shao, *Electrochim. Acta* **207**, 58–65 (2016)
18. T. Zhang, H. Liang, C. Xie, H. Qiu, Z. Fang, L. Wang, H. Yue, G. Chen, Y. Wei, C. Wang, D. Zhang, *Chem. Eng. J.* **326**, 820–830 (2017)
19. W. Dang, F. Wang, Y. Ding, C. Feng, Z. Guo, *J. Alloys Compd.* **690**, 72–79 (2017)
20. H. Rong, G. Xie, S. Cheng, Z. Zhen, Z. Jiang, J. Huang, Y. Jiang, B. Chen, Z.-J. Jiang, *J. Alloys Compd.* **679**, 231–238 (2016)
21. N. Wang, X. Ma, H. Xu, L. Chen, J. Yue, F. Niu, J. Yang, Y. Qian, *Nano Energy* **6**, 193–199 (2014)
22. X. Chen, Y. Zhang, H. Lin, P. Xia, X. Cai, X. Li, X. Li, W. Li, *J. Power Sources* **312**, 137–145 (2016)
23. S. Chen, X. Feng, M. Yao, Y. Wang, F. Wang, Y. Zhang, *Dalton Trans.* **47**, 11166–11175 (2018)
24. G. Huang, S. Xu, Z. Xu, H. Sun, L. Li, *ACS Appl. Mater. Interfaces* **6**, 21325–21334 (2014)
25. X. Lv, Y. Du, Z. Li, Z. Chen, K. Yang, T. Liu, C. Zhu, M. Du, Y. Feng, *Vacuum* **144**, 229–236 (2017)
26. L. Guo, Q. Ru, X. Song, S. Hu, Y. Mo, *J. Mater. Chem. A* **3**, 8683–8692 (2015)
27. Y. Qu, D. Zhang, X. Wang, H. Qiu, T. Zhang, M. Zhang, G. Tian, H. Yue, S. Feng, G. Chen, *J. Alloys Compd.* **721**, 697–704 (2017)
28. G. Li, L. Xu, Y. Zhai, Y. Hou, *J. Mater. Chem. A* **3**, 14298–14306 (2015)
29. X. Gao, J. Wang, D. Zhang, K. Nie, Y. Ma, J. Zhong, X. Sun, *J. Mater. Chem. A* **5**, 5007–5012 (2017)
30. L.-X. Zhang, Y.-L. Wang, H.-F. Jiu, H.-Y. Qiu, H.-Y. Wang, *Ceram. Int.* **41**, 9655–9661 (2015)
31. S. Gu, J. Xu, B. Lu, *Energy Technol.* **4**, 1106–1111 (2016)
32. L. Zhang, S. Zhu, H. Cao, L. Hou, C. Yuan, *Chem. Eur. J.* **21**, 10771–10777 (2015)
33. J. Zeng, Y. Ren, S. Wang, Y. Hao, H. Wu, S. Zhang, Y. Xing, *Inorg. Chem. Front.* **4**, 1730–1736 (2017)
34. W. Zhou, D. Wang, L. Zhao, C. Ding, X. Jia, Y. Du, G. Wen, H. Wang, *Nanotechnology* **28**, 245401 (2017)
35. T. Zhang, H. Qiu, M. Zhang, Z. Fang, X. Zhao, L. Wang, G. Chen, Y. Wei, H. Yue, C. Wang, D. Zhang, *Carbon* **123**, 717–725 (2017)
36. L. Zhou, H.B. Wu, T. Zhu, X.W. Lou, *J. Mater. Chem.* **22**, 827–829 (2012)
37. C. Feng, W. Wang, X. Chen, S. Wang, Z. Guo, *Electrochim. Acta* **178**, 847–855 (2015)
38. H. Li, T. Yang, B. Jin, M. Zhao, E. Jin, S. Jeong, Q. Jiang, *Inorg. Chem. Front.* **6**, 1535–1545 (2019)

**Publisher's Note** Springer Nature remains neutral with regard to jurisdictional claims in published maps and institutional affiliations.